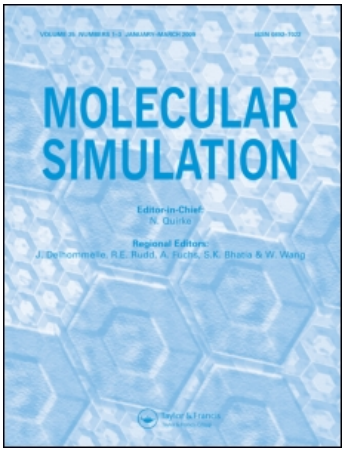

Molecular Simulation
Publication details, including instructions for authors and subscription information:
http://www.informaworld.com/smpp/title~content=t713644482

Electromechanical and Chemical Sensing at the Nanoscale: Molecular Modeling Applications

Amitesh Maiti

To cite this Article Maiti, Amitesh(2004) 'Electromechanical and Chemical Sensing at the Nanoscale: Molecular Modeling Applications', Molecular Simulation, 30: 4, 191 — 198
To link to this Article: DOI: 10.1080/08927020410001659358
URL: http://dx.doi.org/10.1080/08927020410001659358

Molecular Simulation, VOL. 30 (4), 15 April 2004, pp. 191–198

Taylor & Francis
Taylor & Francis Group

Electromechanical and Chemical Sensing at the Nanoscale: Molecular Modeling Applications

AMITESH MAITI*

Accelrys Inc., 9685 Scranton Road, San Diego, CA 92121, USA

(Received July 2003; In final form October 2003)

Atomistic modeling and simulations are becoming increasingly important in the design of new devices at the nanoscale. Of the myriad of potential application areas commonly associated with Nanotechnology, sensors based on carbon nanotubes (CNT) and metal-oxide nanoribbons are one of the closest to commercial reality. In this work, we review some recent molecular modeling investigations on: (1) CNT-based electromechanical sensors, and (2) gas-sensing properties of SnO_2 nanoribbons. Simulation methods include: First-Principles Density Functional Theory (DFT), classical molecular mechanics, and Green's-function-based tight-binding transport.

Keywords: Nanotubes; Nanoribbons; NEMS; DFT; Electronic Transport

INTRODUCTION

Nanotechnology continues to be a rapidly emerging field in which new ideas are being born and discoveries being made at a breathtaking pace. New Materials systems with novel properties are being designed or invented at an incredible rate in laboratories throughout the world. Of the nanosystems, two of the most intensely studied are carbon nanotubes (CNTs) [1–5] and metal-oxide nanoribbons [6–8]. CNTs have been a popular area of research for more than a decade because of the promise of a host of commercial applications [9], including: field emission-based flat panel displays [10–16], novel semiconducting devices in microelectronics [17,18], hydrogen storage devices [19], structural reinforcement agents [20], chemical sensors [21–23], and ultra-sensitive electromechanical sensors [21,24]. Metal-oxide nanoribbons, particularly those synthesized from inexpensive SnO_2 and ZnO [6–8], have been a materials system of great current interest because of potential applications as chemical sensors for pollutant gas species and biomolecules [25–27].

A number of important advances on the experimental front, including the ability to manipulate matter at the nanoscale, are pushing various prototype devices toward commercial reality. At the same time, the well-characterized atomic structures of CNTs and nanoribbons as well as their high degree of structural purity are allowing accurate computer modeling and *in silico* property prediction. This paper is a review of our modeling endeavor in two application areas: (1) CNT-based nano-electromechanical sensors (NEMS); and (2) SnO_2-nanoribbon-based gas sensors. A host of computational techniques are used: density functional theory (DFT)-based first-principles quantum mechanics, classical forcefield-based molecular mechanics (MM), and tight-binding transport based on the recursive Green's function formalism. A brief description of these methods, along with appropriate references, is given in the Appendix.

CNT-BASED NANO-ELECTROMECHANICAL SENSORS (NEMS)

Interest in the application of carbon nanotubes as electromechanical sensors got a significant boost from the pioneering experiment of Tombler *et al.*[24], in which the middle part of the segment of a metallic

*E-mail: amaiti@accelrys.com

ISSN 0892-7022 print/ISSN 1029-0435 online © 2004 Taylor & Francis Ltd
DOI: 10.1080/08927020410001659358

nanotube suspended over a trench was pushed with an AFM tip. Beyond a deformation angle of ~13° the electrical conductance of the tube dropped by more than two orders of magnitude. The effect was found to be completely reversible, i.e. through repeated cycles of AFM-deformation and tip removal, the electrical conductance displayed a cyclical variation with constant amplitude. An interesting explanation was put forward by O(N) tight-binding calculations [28], which show that beyond a critical deformation several C-atoms close to the AFM tip become sp^3-coordinated. This leads to the tying up of π-electrons into localized σ-states, which would explain the large drop in electrical conductance.

The smallest models of CNTs necessary in such simulations typically involve a few thousand atoms, which makes first-principles quantum mechanics simulations unfeasible. Therefore, we carried out a combination of first-principles DFT and classical molecular mechanics to investigate structural changes in a CNT under AFM-deformation. Bond reconstruction, if any, is likely to occur only on the highly deformed, non-straight part of the tube close to the AFM-tip. For such atoms, we used a DFT-based quantum mechanical description (~100–150 atoms including AFM-tip atoms), while the long and essentially straight part away from the middle was described accurately using the universal forcefield (UFF) [29,30].

Because of known differences in electronic response of zigzag and armchair tubes to mechanical deformation, we studied a (12,0) zigzag and a (6,6) armchair tube, each consisting of 2400 atoms. The AFM tip was modeled by a 6-layer deep 15-atom Li-needle normal to the (100) direction, terminating in an atomically sharp tip. To simulate AFM-tip-deformation, the Li-needle was initially aimed at the center of a hexagon on the bottom-side of the middle part of the tube. The Li-needle tip was then displaced by an amount δ toward the tube along the needle-axis, resulting in a deformation angle $\theta = \tan^{-1}(2\delta/L)$, L being the unstretched length of the tube. At each end of the tube, a contact region defined by a unit cell plus one atomic ring (a total of 36 and 60 atoms for the armchair and the zigzag tube, respectively) was then fixed and the whole tube relaxed with the UFF. The whole tube was then relaxed by UFF keeping the needle atoms and the end contact regions of the tube fixed. The contact region atoms were fixed in order to simulate an ideal undeformed semi-infinite carbon nanotube lead, and to ensure that all possible contact modes are coupled to the deformed part of the tube. Following the UFF relaxation, a cluster of 132 C-atoms for the (6,6) tube, and a cluster of 144 C-atoms for the (12,0) tube were cut out from the middle of the tubes. These clusters, referred to below as the *QM clusters* (plus the 15 Li-tip atoms in tip-deformation simulations) were further relaxed with Accelrys' DFT-code DMol^3 [31–34][†], with the end atoms of the cluster plus the Li-tip atoms fixed at their respective classical positions. In order to cut down on CPU requirements, the DFT calculations were performed using the Harris functional [35,36] and the local exchange-correlation potential due to Vosko, Wilk and Nusair [37].

Figure 1 displays the tip-deformed QM-cluster for the (6,6) and the (12,0) tubes at the highest deformation angle of 25° considered in these simulations. Even under such large deformations, there is no indication of sp^3 bonding, and the structure was very similar to what was observed for the (5,5) tube in Ref. [38]. The absence of sp^3 coordination is inferred based on an analysis of nearest-neighbor distances of the atoms with the highest displacements, i.e. the ones closest to the Li-tip. *Although for each of these atoms the three nearest neighbor C–C bonds are stretched to between 1.45–1.75 Å, the distance of the fourth neighbor, required to induce sp^3 coordination, is greater than 2.2 Å for all tubes in our simulations.* The electronic charge density in the region between a C-atom and its fourth nearest neighbor is negligibly small, and none of the C–C–C angles between bonded atoms in the vicinity of the tip deviates by more than a few degrees from 120°, suggesting that the C-atoms near the AFM-tip essentially remain sp^2-coordinated.

Following structural relaxation of the CNTs, we computed the transmission and conductance using the formalism outlined in the Appendix. Our results indicate that the conductance remains essentially constant for the (6,6) armchair tube up to deformation as large as 25°. However, for the (12,0) tube the conductance drops by a factor of ~0.3 at 15°, two orders of magnitude at 20°, and 4 orders of magnitude at $\theta = 25°$. Since sp^3 coordination could be ruled out, what could be the cause for such a large conductance drop in the experiment of Ref. [24], as well as in our simulation on the metallic zigzag tube? Also, why did the armchair tube display no significant drop in conductance even up to large angles of deformation?

A simple explanation emerges if one zooms out from the middle of the tube and looks at the profile of the whole tube under AFM-deformation. One immediately discovers an overall stretching of

[†]See URL: http://www.accelrys.com/mstudio/dmol3.html for information on the latest version of DMol^3.

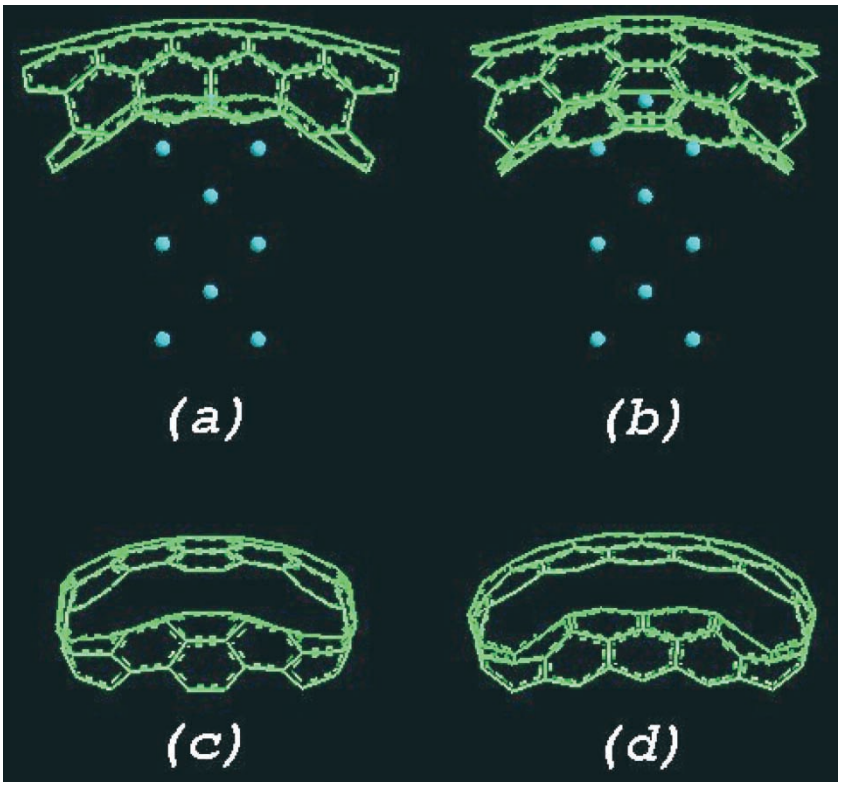

FIGURE 1 DMol^3-relaxed Li-tip-deformed QM clusters for: (a) the (6,6) armchair (132 C-atoms); and (b) the (12,0) zigzag (144 C-atoms), in side views. The deformation angle is 25° for both tubes; (c) and (d) are respective views along the tube length, with the Li-tip hidden for clarity.

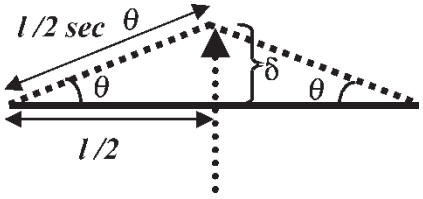

FIGURE 2 Schematic diagram representing deformation with an AFM tip. The tip-deformed tube undergoes a tensile strain. The deformation angle θ is related to the tip displacement (δ) and non-deformed tube-length (L) by $\theta = \tan^{-1}(2\delta/L)$.

the tube under AFM-deformation, as indicated schematically in Fig. 2‡. Figure 3 compares a drop in conductance in the (12,0) tube subjected to: (1) AFM-deformation, and (2) uniform stretching. Such a comparison makes it clear that tensile strain is the main reason behind the conductance drop in an AFM-deformed metallic zigzag tube. We have also verified that the (6,6) armchair tube does not undergo any significant conductance drop upon stretching.

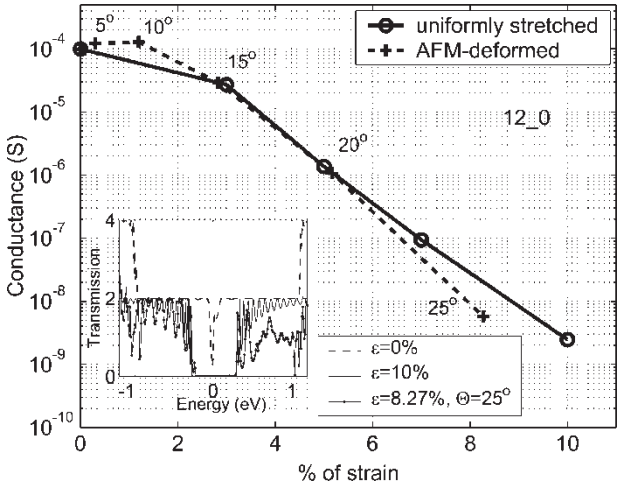

FIGURE 3 Conductance of an AFM-tip-deformed (12,0) tube as compared to the same tube under a uniform stretch. Actual angles of tip-deformation are indicated. The % strain for the AFM-deformed tube is computed from the average C–C bond-stretch in the middle of the straight portion of the tube [40]. The inset shows transmission in the vicinity of the Fermi surface ($E = 0$) for a uniform strain of 10% and a tip-deformation angle of 25°, as compared to the non-deformed tube.

‡For a tube with a very large length-to-diameter ratio, the length L stretches to $\sim L \sec\theta$, θ being the tip-deformation angle [see Fig. 2]. However, for moderately long tubes used in our simulations, the average tensile strain in the straight part of the tube is slightly lower than $(\sec\theta - 1)$.

In order to explain the differences in conductance drops of the armchair (6,6) and the zigzag (12,0) tubes as a function of strain, we turn to the literature where a considerable amount of theoretical work already exists [39–44]. An important result [42] is that the *rate of change* of bandgap as a function of strain depends on the CNT chiral angle θ, more precisely as proportional to $\cos(3\theta)$. Thus, stretched armchair tubes ($\theta = 30^\circ$) do not open any bandgap, and always remain metallic. On the other hand, a metallic ($3n$,0) zigzag tube ($\theta = 0$) can open a bandgap of $\sim$100 meV when stretched by only 1%. This bandgap increases linearly with strain, thus transforming the CNT into a semiconductor at a strain of only a few percent. In general, all metallic tubes with $n_1 - n_2 = 3n$ will undergo the above metal-to-semiconductor transition, the effect being most pronounced in metallic zigzag tubes. An experiment as in Ref. [24] is, thus, expected to show a decrease in conductance upon AFM-deformation for all nanotubes except the armchair tubes.

In addition to the above results for metallic CNTs, theory also predicts that [42] for semiconducting tubes ($n_1 - n_2 \neq 3n$), the bandgap can either increase (for $n_1 - n_2 = 3n - 2$) or decrease (for $n_1 - n_2 = 3n - 1$) with strain. These results have recently prompted more detailed experiments on a set of metallic and semiconducting CNTs deformed with an AFM-tip [45], as well as on CNTs under experimental tensile stretch [46]. Commercial applications from such work could lead to novel pressure sensors, transducers, amplifiers, and logic devices [47].

CHEMICAL SENSORS BASED ON METAL-OXIDE NANORIBBONS

Recent experiments with SnO_2 nanoribbons [48] indicate that these are highly effective in detecting even very small amounts of harmful gases like NO_2. Upon adsorption of these gases, the electrical conductance of the sample decreases by several orders of magnitude. More interestingly, it is possible to get rid of the adsorbates by shining UV light, and the electrical conductance is completely restored to its original value. Such single-crystalline sensing elements have several advantages over conventional thin film oxide sensors: low operating temperatures, no ill-defined coarse grain boundaries, and high active surface-to-volume ratio.

The experimental nanoribbons were synthesized using a novel approach based on a simple thermal-deposition process [6]. Field-emission scanning electron microscopy (FE-SEM) and Transmission Electron microscopy revealed that the ribbons:

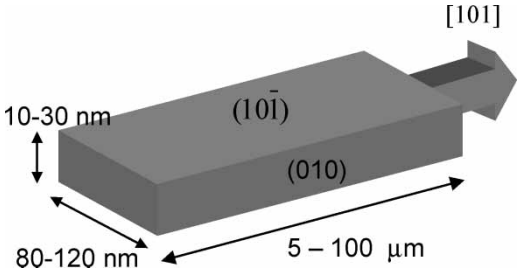

FIGURE 4 Schematic diagram of a SnO_2 nanoribbon, showing typical dimensions, exposed planes, and growth direction.

(1) possess a highly crystalline rutile structure; (2) grow tens of microns long in the $\langle 1\ 0\ 1 \rangle$ direction; (3) display a uniform quasi-rectangular cross-section perpendicular to the growth direction; and (4) present the (1 0 $\bar{1}$) and (0 1 0) rutile planes as surface facets along the growth axis, with dimensions ranging between 80–120 nm by 10–30 nm (Fig. 4). Rutile SnO_2 is a wide-bandgap (3.6 eV) *n*-doped semiconductor, with the intrinsic carrier density determined by the deviation from stoichiometry, primarily in the form of oxygen vacancies [49].

Electron withdrawing groups like NO_2 and O_2 are expected to deplete the conduction electron population in the nanoribbon, thereby leading to a decrease in electrical conductance. To investigate this, we have carried out a first-principles DFT investigation of the adsorption process of NO_2, O_2 and CO on the exposed (1 0 $\bar{1}$) and (0 1 0) surfaces, as well as the edge atoms of a SnO_2 nanoribbon. The DFT code used was $DMol^{3+}$ [31]. We performed all-electron calculations with a double numeric polarized (DNP) basis set, and the gradient-corrected PBE functional [50]. Nanoribbon surfaces were represented in periodic supercells (Fig. 5), and accurate Brillouin zone integration was performed by careful sampling of *k*-points chosen according to the Monkhorst-Pack scheme [51] with a k-point spacing of 0.1 Å^{-1}. In order to estimate charge transfer to adatoms, we computed partial charge on each atom using the Mulliken population analysis [52].

In bulk rutile SnO_2, the Sn-atoms are octahedrally coordinated with six O-neighbors, while each O-atom is a threefold bridge between neighboring Sn-centers. At both (1 0 $\bar{1}$) and (0 1 0) surfaces the Sn-atoms lose an O-neighbor, thereby becoming fivefold coordinated, Fig. 5(a, b). The surface O-atoms become twofold-coordinated bridges connecting neighboring surface Sn-atoms, Fig. 5(a, b). Both surfaces were represented by three layers of Sn, each layer being sandwiched between two O-layers. The bottom SnO_2 layer was fixed in order to simulate the presence of several bulk-like layers in the actual sample. In order to reduce interaction

with periodic images, the surface unit cell was doubled in the direction of the smaller surface lattice constant, and a vacuum of 15 Å was placed normal to the surface. To simulate nanoribbon edges (i.e. lines of intersection of (1 0 $\bar{1}$) and (0 1 0) planes), a structure as in Fig. 5(c) was embedded in a periodic supercell with the smallest repeat period (5.71 Å) along the length of the ribbon, and a vacuum of 15 Å normal to both the (1 0 $\bar{1}$) surface (*y*-axis) and the (0 1 0) surface (*x*-axis). At the nanoribbon edges the Sn-atoms can be either threefold- or fourfold-coordinated, Fig. 5(c).

Details of the results on binding energy and charge transfer are published elsewhere [53]. We summarize the important results below:

(i) All adsorbate structures involve one or more bonds to surface Sn-atoms. The binding energy increases in the sequence (0 1 0) < (1 0 $\bar{1}$) < 3-fold edge < 4-fold edge.
(ii) NO_2 adsorption displays a very rich chemistry because it can either form a single bond to a surface Sn, or can adsorb in the bidented form through two single bonds to neighboring

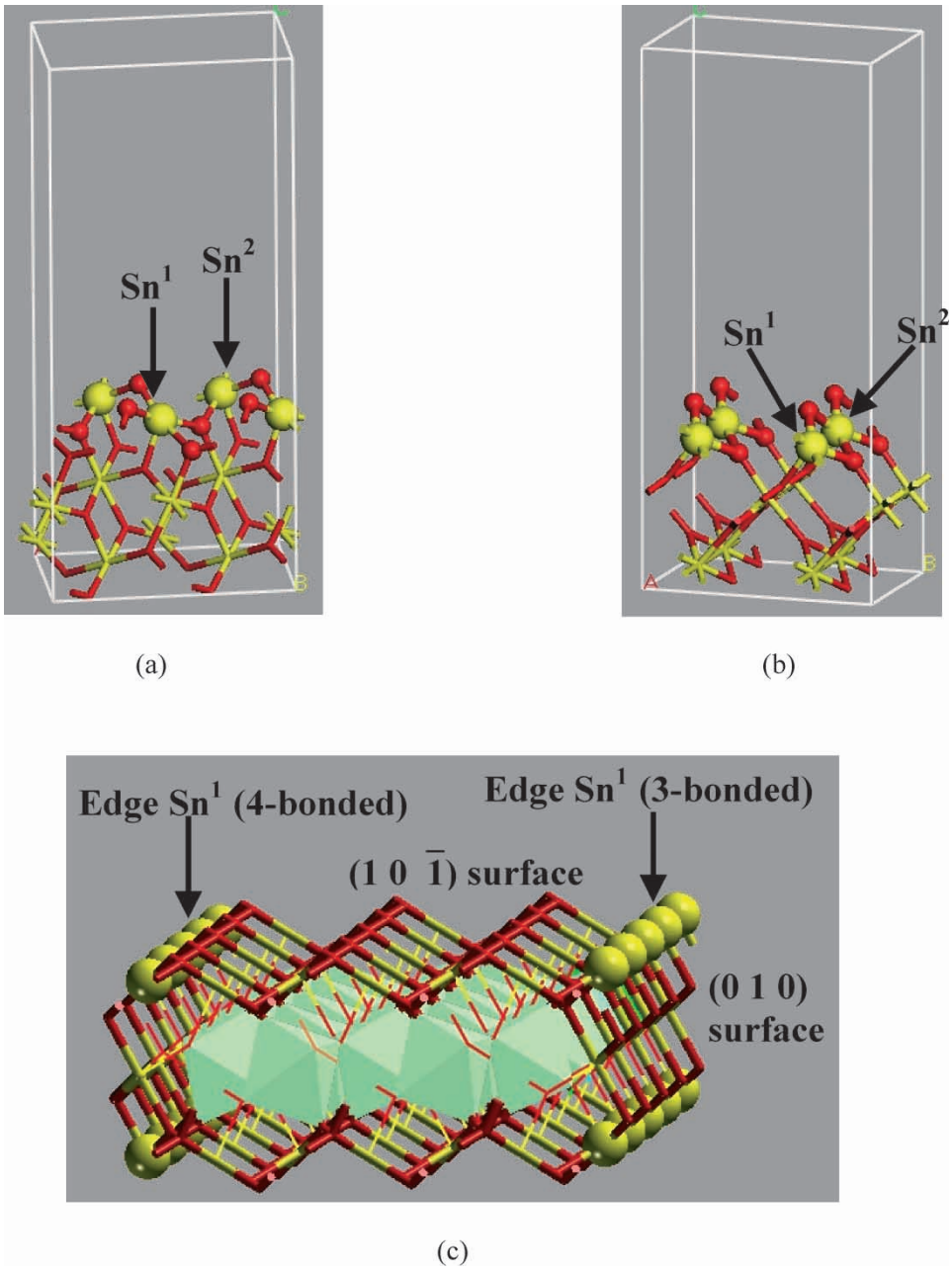

FIGURE 5 Simulation supercells representing exposed surfaces of a SnO_2 nanoribon: (a) (1 0 $\bar{1}$) surface; (b) (0 1 0) surface; and (c) nanoribbon edge. For clarity, the periodic cell is not shown in (c), and the interior atoms are represented by polyhedra. Surface atoms in (a) and (b), and edge atoms in (c) are shown in ball representation. Yellow (larger) balls and Red (smaller) balls represent Sn and O-atoms respectively. Sn^1 and Sn^2 are neighboring Sn-atoms connected with a bridging O. (Colour version available online.)

Sn-atoms. The doubly bonded NO_2 is 2–3 kcal/mol more stable than the single--bonded NO_2, and the binding energies are in general 4–5 kcal/mol higher on the (1 0 $\bar{1}$) surface than on the (0 1 0). Activation barrier between the doubly-bonded and single--bonded structures is expected to be low, which should make the NO_2 species mobile on the exposed faces by performing a series of random walk steps along well-defined rows of Sn-atoms on the surface.

(iii) When two NO_2 molecules meet on the surface, either through random walk as described above, or through the incidence of a second NO_2 from gas phase in the vicinity of an already chemisorbed NO_2, there is a transfer of an O-atom from one NO_2 to the other, thus converting it to a surface NO_3 species. The bidented NO_3 group has a substantially higher binding energy, especially on the (1 0 $\bar{1}$) surface, and should not, therefore, be mobile. The net disproportionation reaction $NO_2 + NO_2 \rightarrow NO_3 + NO$ is well known in chemistry. The resulting NO species is only weakly bound to the surface and should desorb easily. Synchrotron measurements using X-ray absorption near-edge spectroscopy (XANES) have recently confirmed the abundance of NO_3 species on the nanoribbon surface following NO_2 adsorption [53].

(iv) A CO likes to adsorb in the following manner: the C forms two single bonds to the surface—one with a surface Sn and another with a bridging O, while the O of the CO forms a double bond to the C and sticks out of the surface. This way, the C-atoms attains its preferred 4-valency and the O has its bivalency satisfied.

(v) On a defect-free surface (i.e. surface with no O-vacancies), the O_2 molecules can only weakly physisorb. In this configuration, there is no charge transfer to the O_2, and therefore a nanoribbon surface without surface O-vacancies should be insensitive to atmospheric oxygen. However, at O-vacancy sites, the O_2 molecule has a strongly bound chemisorbed structure in the form of a peroxide bridge.

(vi) Both NO_3 groups and chemisorbed O_2 (at O-vacancy sites) accept a significant amount of electronic charge from the surface. Therefore, such adsorbates should lead to the lowering of electrical conductance of the sample. CO, on the other hand, donates a moderate amount of electrons to the surface, and is, therefore, expected to increase the electrical conductance. All these results are consistent with direct experimental measurements of sample conductance [26,48,54].

Acknowledgements

I would like to thank Accelrys Inc. for support of this research. I would also like to acknowledge collaborations with M. P. Anantram and Alexei Svizhenko (NASA, Ames), José Rodriguez (Brookhaven National Lab), Peidong Yang (UC, Berkeley), and Paul Kung and Jan Andzelm (Accelrys) for parts of the work reported here.

APPENDIX: SUMMARY OF COMPUTATIONAL TECHNIQUES

First-principles Density Functional Theory (DFT)

First-principles methods of solving many-electron Schrödinger equation can be broadly classified into two types: those based on the Hartree-Fock method, and those based on the density functional theory (DFT). Due to better scaling with the number of electrons, DFT is quickly becoming the First-Principles technique of choice in technologically important problems. DFT is based on a theorem due to Hohenberg and Kohn [55], which states that all ground state properties are functions of the total electronic charge density $\rho(\mathbf{r})$. The total energy of an electron gas can be formalistically written as a sum of the kinetic, potential (electrostatic), exchange and correlation energies. A practical implementation of this formalism into computer programs was made possible by the local density approximation (LDA) of Kohn and Sham [56], which recast the many-electron problem into a problem of single electrons moving in an average field of the other electrons and ions. The basic formalism has stood the test of time, although important subsequent developments on gradient corrections to the LDA and the exchange-correlation functional have increased the accuracy of DFT significantly. There are several different DFT codes available commercially, differing primarily in the choice of the basis functions in which the electronic wave functions are expanded, and the scheme of integration. For the work reported here, we used the DFT code DMol^3 [31–34]$^+$,[¶] distributed by Accelrys Inc, in which each electronic wave function is expanded in a localized atom-centered basis set defined on a numerical grid.

[¶]See http://www.accelrys.com/doc/life/insight2K/dmol/2_Theory.html#193994 for details of DFT implementation in DMol^3.

In the present work, the electronic wave functions were expanded in a double-numeric polarized (DNP) basis set with a real-space cut-off of 4.0 Å. Such a cut-off reduces computational requirements without significantly sacrificing accuracy, as has been explicitly verified in this and many other numerical experiments. A thermal smear of 0.01 Hartree was applied to obtain faster SCF convergence, without affecting the structure and energetics to any significant degree.

Classical Molecular Mechanics

Simulations on the AFM-deformed nanotubes involved fairly long structures with several thousand atoms. Performing first-principles DFT calculations on systems of such size is prohibitively expensive, and often unnecessary. In such situations, we used a combination of DFT and classical molecular mechanics (MM) with accurate interatomic potentials describing the C–C interactions. The interatomic C–C potential was described by the universal forcefield (UFF) [29], which has previously been used to study the mechanical properties of carbon nanotubes [30]. The Accelrys MM engines used in this work includes the open force field (OFF) module[§] available with the Cerius[2] interface, and the Forcite module[‖] available with the materials studio interface.

Transport Modeling

Computing conductance through a narrow wire is always tricky because contact effects can often overshadow the intrinsic molecular conductance of the wire. However, under the assumption of ideal semi-infinite contacts, we computed the transmission and conductance using the recursive Green's function formalism [57,58] within the framework of a nearest-neighbor sp^3-tight-binding Hamiltonian in a non-orthogonal basis. The parameterization scheme explicitly accounts for effects of strain in the system through a bond-length-dependence of the Hamiltonian and the overlap matrices H_{ij} and S_{ij}, as in Ref. [59]. First, the retarded Green's function G^{R} of the whole nanotube was determined by solving the following equation:

$$(E \cdot S_{ij} - H_{ij} - \Sigma_{\mathrm{L},ij} - \Sigma_{\mathrm{R},ij}) G^{\mathrm{R},jk} = \delta_i^k, \qquad (1)$$

where $\Sigma_{\mathrm{L,R}}$ are the retarded self-energies of the left and the right semi-infinite contacts. The transmission at each energy were then found [60][#] from the equation:

$$T(E) = G^{\mathrm{R},ij} \Gamma_{\mathrm{L},jk} G^{\mathrm{A},kl} \Gamma_{\mathrm{R},li}, \qquad (2)$$

where $\Gamma_{\mathrm{L,R}} = i(\Sigma^{\mathrm{R}}_{\mathrm{L,R}} - \Sigma^{\mathrm{A}}_{\mathrm{L,R}})$ are the couplings to the left and right leads. Finally, the total conductance of the tube was computed using Landauer-Büttiker formula:

$$G = \frac{2e^2}{h} \int_{-\infty}^{\infty} T(E)(-\frac{\partial f_o}{\partial E})\, \mathrm{d}E, \qquad (3)$$

where $f_o(E)$ is the Fermi-Dirac function.

References

[1] Iijima, S. (1991) "Helical microtubules of graphitic carbon", *Nature* **354**, 56.
[2] Iijima, S., Ichihashi, T. and Ando, Y. (1992) "Pentagons, heptagons and negative curvature in graphite microtubule growth", *Nature* **356**, 776.
[3] Ebbesen, T.W. and Ajayan, P.M. (1992) "Large scale synthesis of carbon nanotubes", *Nature* **358**, 220.
[4] Bethune, D.S., *et al.* (1993) "Cobalt-catalysed growth of carbon nanotubes with single-atomic-layer walls", *Nature* **363**, 605.
[5] Iijima, S. and Ichihashi, T. (1993) "Single-shell carbon nanotubes of 1-nm diameter", *Nature* **363**, 603.
[6] Dai, Z.R., Pan, Z.W. and Wang, Z.L. (2001) "Ultra-long single crystalline nanoribbons of tin oxide", *Solid State Commun.* **118**, 351.
[7] Huang, M., Wu, Y., Feick, H., Tran, N., Weber, E. and Yang, P. (2001) "Catalytic growth of zinc oxide nanowires by vapor transport", *Adv. Mater.* **13**, 113.
[8] Huang, M., Mao, S., Feick, H., Yan, H., Wu, Y., Kind, H., Weber, E., Russo, R. and Yang, P. (2001) "Room-temperature ultraviolet nanowire nanolasers", *Science* **292**, 1897.
[9] Articles on nanotubes in *Physics World* **13**, Issue 6 (2000) 29–53.
[10] de Heer, W.A., Chatelain, A. and Ugarte, D. (1995) "A carbon nanotube field-emission electron source", *Science* **270**, 1179.
[11] Rinzler, A.G., *et al.* (1995) "Unraveling nanotubes: field emission from an atomic wire", *Science* **269**, 1550.
[12] Collins, P.G. and Zettl, A. (1996) "A simple and robust electron beam source from carbon nanotubes", *Appl. Phys. Lett.* **69**, 1969.
[13] Gulyaev, Y.V., *et al.* (1997) "Work function estimate for electrons emitted from nanotube carbon cluster films", *J. Vac. Sci. Technol., B* **15**, 422.
[14] Fan, S., *et al.* (1997) "Self-oriented regular arrays of carbon nanotubes and their field emission properties", *Science* **283**, 512.
[15] Küttel, O.M., Groenig, O., Emmenegger, C. and Schlapbach, L. (1998) "Electron field emission from phase pure nanotube films grown in a methane/hydrogen plasma", *Appl. Phys. Lett.* **73**, 2113.
[16] Fransen, M.J., van Rooy, Th. L. and Kruit, P. (1999) "Field emission energy distributions from individual multi-walled carbon nanotubes", *Appl. Surf. Sci.* **146**, 312.
[17] Tans, S.J., Verchueren, A.R.M. and Dekker, C. (1998) "Room-temperature transistor based on a single carbon nanotube", *Nature* **393**, 49.
[18] de Heer, W.A. and Martel, R. (2000) "Industry sizes up nanotubes", *Physics World*, 49, June 2000.

[§]See http://www.accelrys.com/cerius2/off.html
[‖]See http://www.accelrys.com/mstudio/ms_modeling/forcite.html
[#]In the Eqs.(1–3), summation is performed over the repeating roman indices. The lower and upper indices denote covariant and contravariant components of a tensor.

[19] Liu, C., *et al.* (1999) "Hydrogen storage in single-walled carbon nanotubes at room temperature", *Science* **286**, 1127.
[20] Wong, *et al.* (1997) "Nanobeam mechanics: elasticity, strength, and toughness of nanorods and nanotubes", *Science* **277**, 1971.
[21] Dai, H. (2000) "Controlling nanotube growth", *Phys. World*, 43, June 2000.
[22] Kong, J., *et al.* (2000) "Nanotube molecular wires as chemical sensors", *Science* **287**, 622.
[23] Collins, P.G., *et al.* (2000) "Extreme oxygen sensitivity of electronic properties of carbon nanotubes", *Science* **287**, 1801.
[24] Tombler, T.W., *et al.* (2000) "Reversible electromechanical characteristics of carbon nanotubes under local-probe manipulation", *Nature* **405**, 769.
[25] Cui, Y., Wei, Q., Park, H. and Lieber, C.M. (2001) "Nanowire nanosensors for highly sensitive and selective detection of biological and chemical species", *Science* **293**, 1289.
[26] Comini, E., Faglia, G., Sberveglieri, G., Pan, Z. and Wang, Z.L. (2002) "Stable and highly sensitive gas sensors based on semiconducting oxide nanobelts", *Appl. Phys. Lett.* **81**, 1869.
[27] Favier, F., Walter, E.C., Zach, M.P., Benter, T. and Penner, R.M. (2001) "Hydrogen sensors and switches from electrodeposited palladium mesowire arrays", *Science* **293**, 2227.
[28] Liu, L., Jayanthi, C.S. and Dai, H. (2000) "Controllable reversibility of an sp^2 to sp^3 transition of a single wall nanotube under the manipulation of an AFM tip: a nanoscale electromechanical switch?", *Phys. Rev. Lett.* **84**, 4950.
[29] Rappe, A.K., Casewit, C.J., Colwell, K.S., Goddard, W.A. and Skiff, W.M. (1992) "UFF, a full periodic table force field for molecular mechanics and molecular dynamics simulations", *J. Am. Chem. Soc.* **114**, 10024.
[30] Yao, N. and Lordi, V. (1998) "Young's modulus of single-walled carbon nanotubes", *J. Appl. Phys.* **84**, 1939.
[31] Delley, B. (1990) "An all-electron numerical method for solving the local density functional for polyatomic molecules", *J. Chem. Phys* **92**, 508.
[32] Delley, B. (1996) "Fast calculation of electrostatics in crystals and large molecules", *J. Phys. Chem.* **100**, 6107.
[33] Delley, B. (1998) "A scattering theoretic approach to scalar relativistic corrections on bonding", *Int. J. Quantum Chem.* **69**, 423.
[34] Delley, B. (2000) "From molecules to solids with the $DMol^3$ approach", *J. Chem. Phys.* **113**, 7756.
[35] Lin, Z. and Harris, J. (1992) "A localized-basis scheme for molecular dynamics", *J. Phys. Condens. Matter* **4**, 1055.
[36] Li, X.P., Andzelm, J.W., Harris, J. and Chaka, A.M. (1996) "A fast density-functional method for chemistry", In: Laird, B.B., Ross, R.B. and Zeigler, T., eds, *Chemical Applications of Density Functional Theory* ACS Symposium Series, **629**, pp 388–401.
[37] Vosko, S.H., Wilk, L. and Nusair, M. (1980) "Accurate spin-dependent electron liquid correlation energies for local spin density calculations: a critical analysis", *Can. J. Phys.* **58**, 1200.
[38] Maiti, A. (2001) "Application of carbon nanotubes as electromechanical sensors—results from first-principles simulations", *Phys. Stat. Sol., B* **226**, 87.
[39] Kane, C.L. and Mele, E.J. (1997) "Size, shape, and low energy electronic structure of carbon nanotubes", *Phys. Rev. Lett.* **78**, 1932.
[40] Heyd, R., Charlier, A. and McRae, E. (1997) "Uniaxial-stress effects on the electronic properties of carbon nanotubes", *Phys. Rev., B* **55**, 6820–6824.
[41] Yang, L., Anantram, M.P., Han, J. and Lu, J.P. (1999) "Band-gap change of carbon nanotubes: effect of small uniaxial and torsional strain", *Phys. Rev., B* **60**, 13874–13878.
[42] Yang, L. and Han, J. (2000) "Electronic structure of deformed carbon nanotubes", *Phys. Rev. Lett.* **85**, 154–157.
[43] Kleiner, A. and Eggert, S. (2001) "Band gaps of primary metallic carbon nanotubes", *Phys. Rev., B* **63**, 073408.
[44] Maiti, A., Svizhenko, A. and Anantram, M.P. (2002) "Electronic transport through carbon nanotubes: effects of structural deformation and tube chirality", *Phys. Rev. Lett.* **88**, 126508.
[45] Minot, E.D., *et al.* (2003) "Tuning carbon nanotube band gaps with strain", *Phys. Rev. Lett.* **90**, 156401.
[46] Cao, J., Wang, Q. and Dai, H. (2003) "Electromechanical properties of metallic, quasimetallic, and semiconducting carbon nanotubes under stretching", *Phys. Rev. Lett.* **90**, 157601.
[47] Maiti, A. (2003) "Carbon nanotubes: bandgap engineering with strain", *Nat. Mater. (Lond.)* **2**, 440.
[48] Law, M., Kind, H., Kim, F., Messer, B. and Yang, P. (2002) "Photochemical sensing of NO_2 with SnO_2 nanoribbon nanosensors at room temperature", *Angew. Chem. Int. Ed.* **41**, 2405.
[49] Founstadt, C.G. and Rediker, R.H. (1971) "Electrical properties of high-quality stannic oxide crystals", *J. Appl. Phys.* **42**, 2911.
[50] Perdew, J.P., Burke, K. and Ernzerhof, M. (1996) "Generalized gradient approximation made simple", *Phys. Rev. Lett.* **77**, 3865.
[51] Monkhorst, H.J. and Pack, J.D. (1976) "Special points for Brillouin-zone integrations", *Phys. Rev., B* **13**, 5188.
[52] Szabo, A. and Ostlund, N.S. (1996) *Modern Quantum Chemistry* (Dover, New York), p 151.
[53] Maiti, A., Rodriguez, J., Law, M., Kung, P., McKinney, J. and Yang, P. (2003) "SnO_2 nanoribbons as NO_2 sensors: insights from first-principles calculations", *Nano Lett.* **3**(8), 1025.
[54] Kind, H., Yan, H., Law, M., Messer, B. and Yang, P. (2002) "Nanowire ultraviolet photodetectors and optical switches", *Adv. Mater.* **14**, 158.
[55] Hohenberg, P. and Kohn, W. (1964) "Inhomogeneous electron gas", *Phys. Rev.* **136**, B864.
[56] Kohn, W. and Sham, L.J. (1965) "Self-consistent equations including exchange and correlation effects", *Phys. Rev.* **140**, A1133.
[57] Datta, S. (1997) *Electronic transport in mesoscopic systems* (Cambridge University Press).
[58] Svizhenko, A., Anantram, M.P., Govindan, T.R., Biegel, B. and Venugopal, R. (2002) "Two-dimensional quantum mechanical modeling of nanotransistors", *J. Appl. Phys.* **91**, 2343.
[59] Papaconstantopoulos, D.A., Mehl, M.J., Erwin, S.C. and Pederson, M.R. (1998) In: Turchi, P.E.A., Gonis, A. and Colombo, L., eds, *Tight-Binding Approach to Computational Materials Science*, MRS Proceedings, (Materials Research Society, Warrendale, PA) **491**.
[60] Lohez, D. and Lanoo, M. (1983) "Generalization of the Green's-functions formalism to nonorthogonal orbitals: application to amorphous SiO_2", *Phys. Rev., B* **27**, 5007.